



## Nickel-nitride composite: An eco-friendly and efficient alternative to platinum for electrocatalytic hydrogen production

Shuqin Liang<sup>b,e,g,1</sup>, Huashuai Hu<sup>a,1</sup>, Jue Liu<sup>c,1</sup>, Hangjia Shen<sup>b</sup>, Qiao Li<sup>b</sup>, Nianxiang Qiu<sup>b</sup>, HaiChuan Guo<sup>b</sup>, Xuyun Guo<sup>d</sup>, Shiyu Du<sup>b</sup>, Ye Zhu<sup>d</sup>, Jian Liu<sup>e,\*</sup>, J. Paul Attfield<sup>f,\*</sup>, Minghui Yang<sup>a,b,\*\*</sup>

<sup>a</sup> School of Environmental Science and Technology, Dalian University of Technology, Dalian 116024, China

<sup>b</sup> Ningbo Institute of Materials Technology and Engineering, Chinese Academy of Sciences, Ningbo 315201, China

<sup>c</sup> Neutron Scattering Division, Oak Ridge National Laboratory, Oak Ridge, TN 37831, United States

<sup>d</sup> Department of Applied Physics, Research Institute for Smart Energy, The Hong Kong Polytechnic University, Hung Hom, Hong Kong, China

<sup>e</sup> State Key Laboratory of Heavy Oil Processing and Beijing Key Lab of Oil & Gas Pollution Control, China University of Petroleum, Beijing 102249, China

<sup>f</sup> Centre for Science at Extreme Conditions and School of Chemistry, University of Edinburgh, King's Buildings, Mayfield Road, Edinburgh EH9 3JZ, UK

<sup>g</sup> College of Chemistry and Chemical Engineering, Dezhou University, Dezhou 253023, China



### ARTICLE INFO

#### Keywords:

Hydrogen evolution reaction  
Metal nitride  
Electrocatalysts  
Ultra-high stability  
Electronic redistribution

### ABSTRACT

Water electrolysis using the hydrogen evolution reaction (HER) is a promising method for sustainable hydrogen production. Platinum-based catalysts have traditionally been the most efficient HER catalysts, but their scarcity and sluggish water dissociation limit their practical applications. Here we report on a novel superhydrophilic catalyst of nickel supported on nickel molybdenum nitride ( $\text{Ni}/\text{Ni}_{0.8}\text{Mo}_{4.2}\text{N}_6$ ) that outperforms platinum-based nanomaterials. Despite the low catalytic activity of Ni or  $\text{Ni}_{0.8}\text{Mo}_{4.2}\text{N}_6$  alone, their optimized composite exhibits exceptional HER activity, with respective 500% and 150% increases in the exchange current and turnover frequency compared to commercial Pt/C. Density of states calculations reveal a decrease in electron density of the supported nickel in  $\text{Ni}/\text{Ni}_{0.8}\text{Mo}_{4.2}\text{N}_6$ , leading to a lower free energy of the HER. These findings demonstrate a powerful electron-engineering strategy for designing supported electrocatalysts with outstanding performance for the HER and related processes.

### 1. Introduction

Hydrogen is increasingly regarded as a versatile and eco-friendly energy source to help achieve net-zero targets for  $\text{CO}_2$  emissions [1,2]. Electrochemical water-splitting using renewable electricity from sources such as solar and wind power can offer 'green' hydrogen with no  $\text{CO}_2$  emissions [3,4]. The efficiency of such technology depends on the selectivity, intrinsic activity, and stability of the electrocatalysts used for the water splitting reactions. Pt is currently the dominant electrocatalyst for cathodic HER due to its almost perfect Gibbs free energy for  $\text{H}^*$  adsorption ( $\Delta G_{\text{H}} \approx 0$ ) [5–8]. However, the scarcity [9,10] and resulting high costs of Pt limit its sustainable use for practical applications, and in industrially-relevant alkaline conditions the activity is hindered by a sluggish water dissociation step [11–13] leading to low efficiencies in

both water-alkali and chlor-alkali electrolyzers [2].

As alternatives to Pt, nickel (Ni) based electrocatalysts are known to efficiently cleave H-OH bonds [14] and find use as industrial HER catalysts in basic solutions [15]. However, these materials have shortcomings as intrinsically hydrophobic surfaces make infiltration of aqueous electrolyte difficult [16], and strong adsorption of  $\text{H}^*$  at active sites impedes the progress of HER [5,17]. Various strategies such as strain engineering [18–20], electronic regulation [21–23], and hydrogen spillover effects [24–27] have been employed to optimize the properties of nickel based catalysts, but their activity has remained inferior to that of Pt [8]. Other active HER catalysts such as metal nitrides with excellent corrosion resistance, electrical conductivity and Pt-like electronic structures, have also been discovered [28,29], but to date no catalyst that outperforms Pt in terms of overpotential and

\* Corresponding authors.

\*\* Corresponding author at: School of Environmental Science and Technology, Dalian University of Technology, Dalian 116024, China.

E-mail addresses: [liujian@cup.edu.cn](mailto:liujian@cup.edu.cn) (J. Liu), [j.p.attfield@ed.ac.uk](mailto:j.p.attfield@ed.ac.uk) (J.P. Attfield), [myang@dlut.edu.cn](mailto:myang@dlut.edu.cn) (M. Yang).

<sup>1</sup> These authors contributed equally to this work.

current density has been reported.

We have explored two chemical strategies for improving the performance of  $\text{Mo}_5\text{N}_6$  which was previously reported as a promising HER catalyst [28]; Ni-doping and introducing supported Ni nanoparticles. Ni doping has previously been used to improve properties in  $\text{MoN}_x$  [30,31]. Supported Ni nanoparticles on metal nitrides (such as  $\text{MoN}$  [32] and  $\text{Ni}_3\text{N}$  [33]) are also exhibit good HER activity. A combination of both strategies is found to give an outstanding  $\text{Ni}/\text{Ni}_{0.8}\text{Mo}_{4.2}\text{N}_6$  composite catalyst which exhibits a superhydrophilic surface with nickel nanoparticles uniformly dispersed on  $\text{Ni}_{0.8}\text{Mo}_{4.2}\text{N}_6$  nanosheets. Electron transfer from Ni to  $\text{Ni}_{0.8}\text{Mo}_{4.2}\text{N}_6$  improves the water activation and weakens the adsorption of  $\text{H}^*$  on Ni, and hence dramatically enhances the activity of Ni towards HER. As a precious-metal-free material for HER in alkaline solution,  $\text{Ni}/\text{Ni}_{0.8}\text{Mo}_{4.2}\text{N}_6$  exhibits a small overpotential (20 mV at 10 mA cm<sup>-2</sup>), high turnover frequency (TOF = 0.29 s<sup>-1</sup> at 50 mV overpotential) and exchange current density ( $J_0 = 2.89$  mA cm<sup>-2</sup>), and robust stability (only 26 mV deactivation after 1000 h operation), outperforming the benchmark commercial Pt/C catalyst.

## 2. Experimental section

### 2.1. Synthesis of materials

In a typical preparation of  $\text{Ni}/\text{Ni}_{0.8}\text{Mo}_{4.2}\text{N}_6$  catalyst by hydrothermal method, 0.746 g nickel acetate ( $\text{Ni}(\text{CH}_3\text{COO})_2 \cdot 4 \text{ H}_2\text{O}$ ) and 0.241 g sodium molybdate dihydrate ( $\text{Na}_2\text{MoO}_4 \cdot 2 \text{ H}_2\text{O}$ ) are dispersed into 50 mL water/ethylene glycol (Ni:Mo molar ratio = 3:1; water:ethylene glycol volume ratio = 1:1). After ultrasonic dissolution, the solution is poured into the autoclave and the temperature and time are set to 120 °C and 12 h, respectively, for the synthesis of Ni-Mo precursors (Fig. S1a). After cooling to room temperature, wash repeatedly with ethanol and water until the filtrate becomes colorless. The resulting sample is then dried sufficiently. The precursor is calcined in a tube furnace under a flowing  $\text{NH}_3$  atmosphere. The temperature is raised at a rate of 5 °C min<sup>-1</sup> until it reaches 500 °C and then maintained for 4 h. The obtained black product is labeled as  $\text{Ni}/\text{Ni}_{0.8}\text{Mo}_{4.2}\text{N}_6$  (Fig. S1b). For comparison, the  $\text{Ni}_{0.8}\text{Mo}_{4.2}\text{N}_6$  is prepared by treating  $\text{Ni}/\text{Ni}_{0.8}\text{Mo}_{4.2}\text{N}_6$  in sulfuric acid (0.5 M) for 2 h. Metallic Ni can also be synthesized through a hydrothermal reaction in the absence of  $\text{Na}_2\text{MoO}_4 \cdot 2 \text{ H}_2\text{O}$ , by flowing a mixture of  $\text{H}_2/\text{Ar}$  (5%  $\text{H}_2$ ) over the reactants at a temperature of 500 °C for 2 h, with a heating rate of 5 °C min<sup>-1</sup>. All the reagents were purchased from Sinopharm Chemical Reagent in analytical grade and used as received without further purification.

### 2.2. Materials characterization

Powder X-ray diffraction measurements were carried out using the Rigaku Miniflex 600 instrument with  $\text{Cu K}\alpha$  radiation ( $\lambda = 1.54178 \text{ \AA}$ ). The scanning range was 10–80° at 1° min<sup>-1</sup>. Morphologies and microstructures were characterized by a scanning electron microscope (SEM, Hitachi S-4800) and transmission electron microscope (TEM, FEI Tecnai F20). X-ray photoelectron spectroscopy (XPS) was used to analyze surface valence with a VG ESCALAB MKII instrument and  $\text{Mg K}\alpha$  excitation source. For the XPS analysis, carbon was used as an internal standard with a binding energy of C1s = 284.8 eV. The content of the metal in electrolyte before and after stability are tested by the inductively coupled plasma optical emission spectrometry (ICP-OES) on SPECTRO ARCOS. The content of oxygen and nitrogen are tested by oxygen and nitrogen analyzer (HORIBA EMGA-620 W). The contact angle is measured by Data physics scientific OCA25 Surface Analyser at room temperature. XANES (X-ray absorption near-edge structure) spectra for Ni K-edge were obtained at BL14W1 beamline in Shanghai Synchrotron Radiation Facility (SSRF) using transmission mode. The spectra were collected in a range spanning approximately 200 eV below to 800 eV above the edge, with a step size of 0.5 eV in the near-edge region. The dwell time for each step was set to 1 s. At the Spallation Neutron Source

of Oak Ridge National Laboratory, data on powder neutron diffraction were gathered using the NOMAD beamline [34]. Further details regarding the experimental and data processing procedures can be found in the [Supporting Information](#).

### 2.3. Electrochemical tests

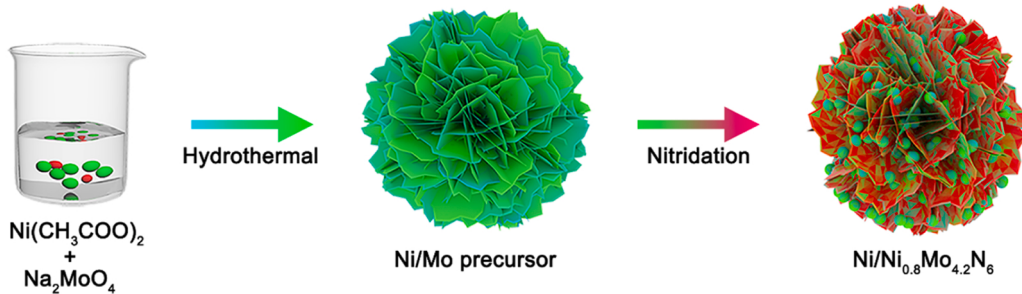
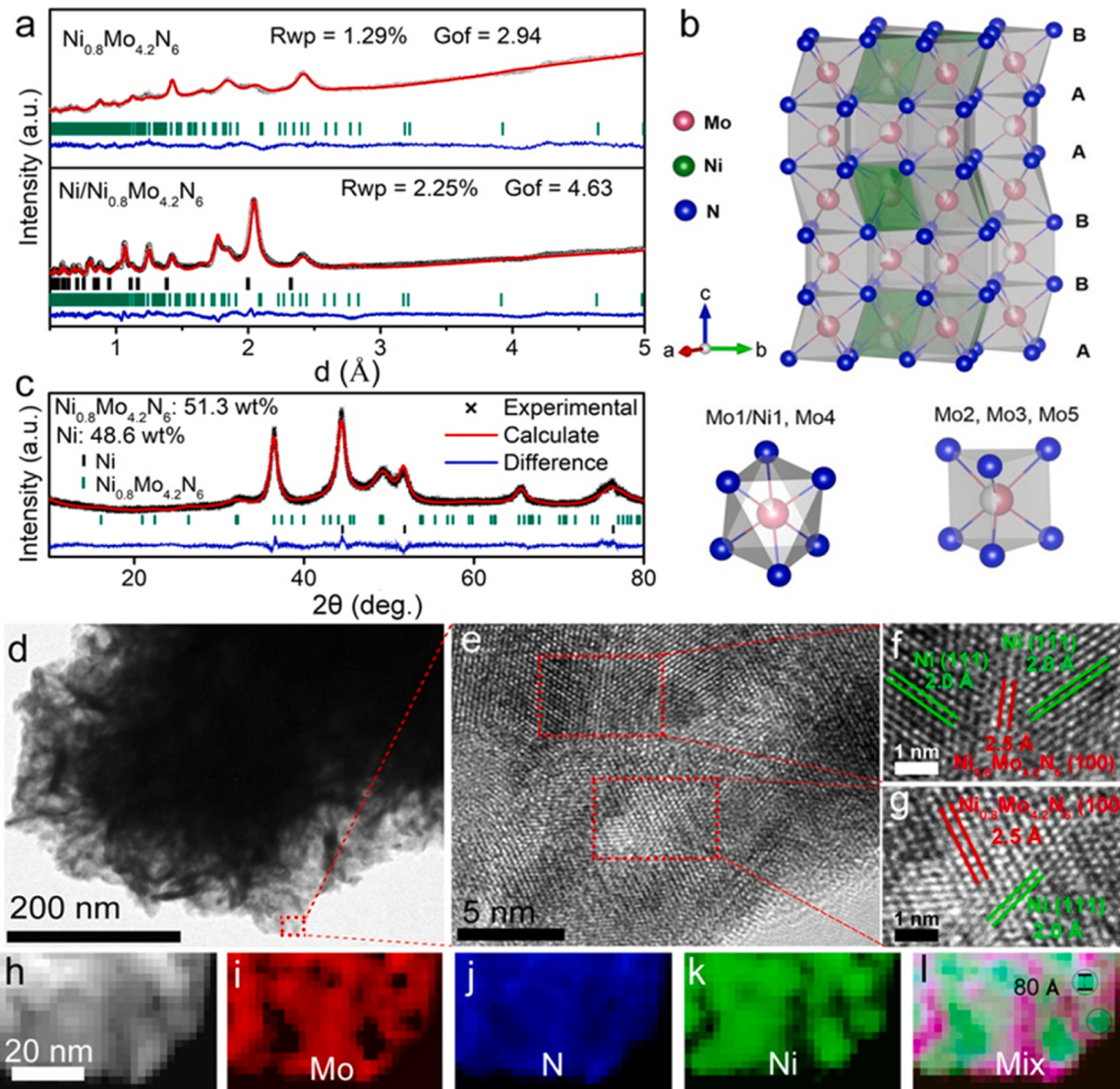
For the experiment, a graphite rod served as the counter electrode while  $\text{Ag}/\text{AgCl}$  (saturated KCl aqueous solution) was used as the reference electrode. To prepare the working electrode, a catalyst ink was created by dispersing the catalyst in a 1:1 mixture of water and isopropyl alcohol with a concentration of 8.0 mg mL<sup>-1</sup>. A small amount (10  $\mu\text{L}$ , 5.0 wt%) of Nafion is added to serve as a binder. After sonication for 30 min to ensure a uniform mixture, 10.0  $\mu\text{L}$  of the ink is applied to a polished glassy carbon electrode (diameter: 5.0 mm). More information about testing the performance of all electrocatalysts and calibrating the reference electrode in the HER experiment is available in the [Supporting Information](#).

## 3. Results and Discussion

The  $\text{Ni}/\text{Ni}_{0.8}\text{Mo}_{4.2}\text{N}_6$  composite and separate  $\text{Ni}_{0.8}\text{Mo}_{4.2}\text{N}_6$  and Ni nanoparticle samples were generated through hydrothermal chemistry as described in [Scheme 1](#). Neutron diffraction (Fig. 1a) demonstrates that the former sample is a composite of Ni and  $\text{Ni}_{0.8}\text{Mo}_{4.2}\text{N}_6$ . The structure refinement results show that Ni has been substituted into the hexagonal  $\text{Mo}_5\text{N}_6$  structure, with the refined composition of  $\text{Ni}_{0.8}\text{Mo}_{4.2}\text{N}_6$  (space group,  $P6_3/m$ ;  $a = 4.9443(8)$ ,  $c = 11.1280(2) \text{ \AA}$ ), which comprises alternate layers of  $\text{MoN}_6$  triangular prisms and octahedra. Ni partially occupies an octahedral site but shifts towards a trigonal prismatic site (Fig. 1b). Powder X-ray diffraction (XRD) in Fig. 1c shows that cubic Ni and hexagonal  $\text{Ni}_{0.8}\text{Mo}_{4.2}\text{N}_6$  phases are both observed for the  $\text{Ni}/\text{Ni}_{0.8}\text{Mo}_{4.2}\text{N}_6$  composite (as compared to patterns for the individual components in Fig. S2). Rietveld XRD analysis shows that the content of cubic nickel is 48.6 wt%, in agreement with ICP-OES results ([Table S1](#)). The Ni particle size in  $\text{Ni}/\text{Ni}_{0.8}\text{Mo}_{4.2}\text{N}_6$  calculated from the Scherrer formula is 8.0 nm, smaller than that for the pristine Ni sample (30 nm). Scanning electron microscope (SEM) shows the  $\text{Ni}/\text{Ni}_{0.8}\text{Mo}_{4.2}\text{N}_6$  composite to have a marigold-like morphology (Fig. S1).

The overlapping crystal lattices (Fig. 1d-g) suggests that the nano-domains of supported Ni and  $\text{Ni}_{0.8}\text{Mo}_{4.2}\text{N}_6$  are contiguous. High-angle annular dark field scanning transmission electron microscopy (HAADF-STEM) and elemental mapping shows the highly dispersed nature of the Ni nanoparticles (NiPs) on the composite surface ([Figs. 1h-l](#) and [S3–S4](#)). The ~8.0 nm NiPs domains visible in [Fig. 1l](#) evidence a high specific surface area ( $S_{\text{BET}}$ ) of  $53 \text{ m}^2 \text{ g}^{-1}$ , larger than that of the pristine Ni ( $23 \text{ m}^2 \text{ g}^{-1}$ ). The STEM images in [Fig. S5](#) reveal that homogeneously dispersed salient NiPs on  $\text{Ni}/\text{Ni}_{0.8}\text{Mo}_{4.2}\text{N}_6$  disappear during acidic etching with the formation of mesopore for  $\text{Ni}_{0.8}\text{Mo}_{4.2}\text{N}_6$ . The diameter of the pores is 8 nm ([Fig. S6](#) and [Table S2](#)), which is exactly the same as the size of the NiPs.

Compared to  $\text{Ni}_{0.8}\text{Mo}_{4.2}\text{N}_6$ , the negative shift in binding energy for the Mo 3d core level in [Fig. 2a](#) suggests an electron rich state of Mo in  $\text{Ni}/\text{Ni}_{0.8}\text{Mo}_{4.2}\text{N}_6$  [35]. Meanwhile, the electron transfers from Ni to the adjacent  $\text{Ni}_{0.8}\text{Mo}_{4.2}\text{N}_6$  (suggested by the positive binding energy shift observed for the Ni 2p core level relative to metallic Ni in [Fig. 2b](#)) leads to a loss of electron charge density on the Ni. Moreover, compared with  $\text{Ni}/\text{Ni}_{0.8}\text{Mo}_{4.2}\text{N}_6$ , the oxidation peak of Ni 2p in  $\text{Ni}_{0.8}\text{Mo}_{4.2}\text{N}_6$  shows a partial positive shift, which is consistent with Mo 3d XPS. [Fig. 2c](#) shows the Ni K-edge X-ray adsorption near-edge structure (XANES) spectra of the samples compared to Ni foil. The absorption edge of  $\text{Ni}/\text{Ni}_{0.8}\text{Mo}_{4.2}\text{N}_6$  locates very close to that of the Ni foil indicates that Ni in  $\text{Ni}/\text{Ni}_{0.8}\text{Mo}_{4.2}\text{N}_6$  resembles its metallic state [17]. However, the enhanced white line intensity and slight shift toward higher energy of the absorption edge (inset [Fig. 2c](#)) suggest that Ni in  $\text{Ni}/\text{Ni}_{0.8}\text{Mo}_{4.2}\text{N}_6$  has a partial positive charge [36]. The confirmed electron-poor Ni supported on

Scheme 1. Schematic diagram of the synthesis for the Ni/Ni<sub>0.8</sub>Mo<sub>4.2</sub>N<sub>6</sub> composite.

**Fig. 1.** (a) Neutron diffraction patterns and Rietveld refinement of  $\text{Ni}_{0.8}\text{Mo}_{4.2}\text{N}_6$  and  $\text{Ni}/\text{Ni}_{0.8}\text{Mo}_{4.2}\text{N}_6$ . (b) Crystal structure of  $\text{Ni}_{0.8}\text{Mo}_{4.2}\text{N}_6$ . (c) The Rietveld refined XRD ( $\lambda = 1.54178 \text{\AA}$ , Cu K $\alpha$ ) pattern of  $\text{Ni}/\text{Ni}_{0.8}\text{Mo}_{4.2}\text{N}_6$ . (d-g) The TEM and HR-TEM images. (h-l) HAADF-STEM image and the energy dispersive X-ray spectroscopy (EDS) element mapping for Ni, Mo, N element.

$\text{Ni}_{0.8}\text{Mo}_{4.2}\text{N}_6$  is important in such systems to weaken  $\text{H}^*$  adsorption and thus boost the HER [21,22,37].

As HER is a gas–liquid–solid three-phase process, a superhydrophilic surface is favorable to promote the infiltration of aqueous electrolyte and facilitate mass transfer [16,38,39]. In contrast to the Pt/C (20 wt%) catalyst which is hydrophobic, liquid–solid contact-angle measurements in Fig. 2d and supplementary videos reveal that  $\text{Ni}/\text{Ni}_{0.8}\text{Mo}_{4.2}\text{N}_6$  is

superhydrophilic. The dispersion of Ni nanostructures on the surface of the nitride, as well as the highly porous marigold structure, aids the structural superhydrophilicity, beyond that of the nitride or metallic Ni alone (Fig. S7).

HER activity of the  $\text{Ni}/\text{Ni}_{0.8}\text{Mo}_{4.2}\text{N}_6$  composite in comparison to the individual Ni and  $\text{Ni}_{0.8}\text{Mo}_{4.2}\text{N}_6$  components and a benchmark Pt/C (20 wt%) catalyst has been measured by linear sweep voltammetry

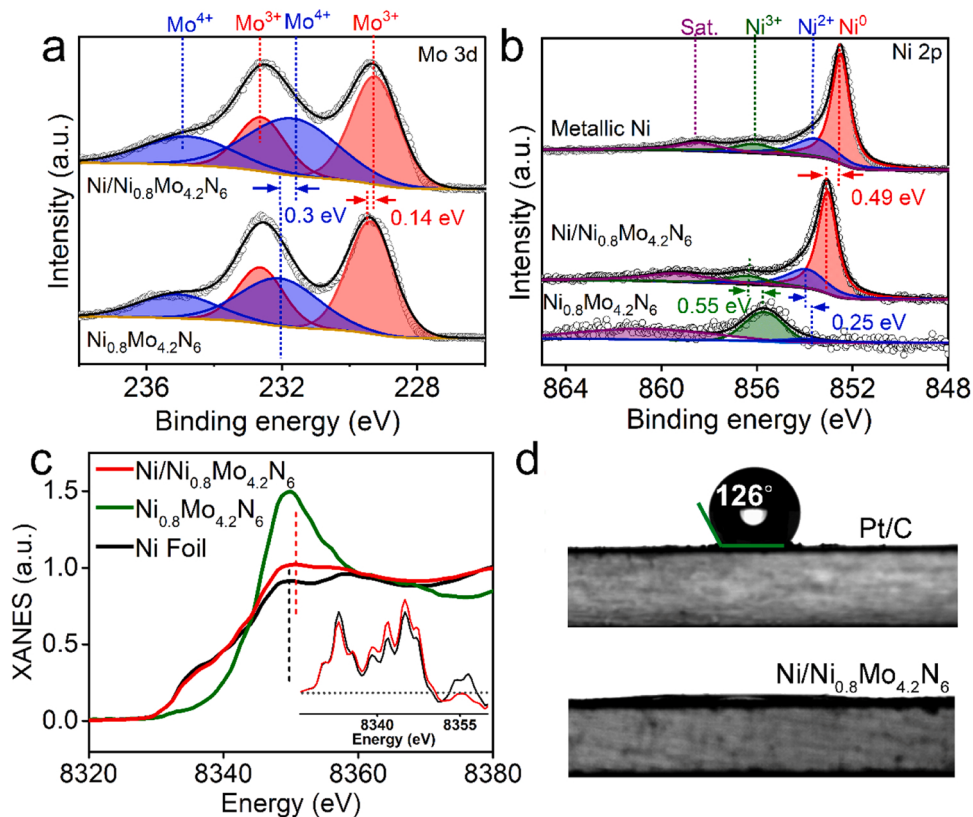


**Fig. 2.** (a) Mo 3d X-ray photoelectron spectroscopy (XPS) spectra of  $\text{Ni}_{0.8}\text{Mo}_{4.2}\text{N}_6$  and  $\text{Ni}/\text{Ni}_{0.8}\text{Mo}_{4.2}\text{N}_6$ . (b) Ni 2p XPS spectra of metallic Ni,  $\text{Ni}/\text{Ni}_{0.8}\text{Mo}_{4.2}\text{N}_6$  and  $\text{Ni}_{0.8}\text{Mo}_{4.2}\text{N}_6$ . (c) Ni K-edge XANES spectra for the  $\text{Ni}_{0.8}\text{Mo}_{4.2}\text{N}_6$  and  $\text{Ni}/\text{Ni}_{0.8}\text{Mo}_{4.2}\text{N}_6$  in comparison with the reference compounds Ni foil (inset: expanded view of Ni K-edge pre-edge). (d) The contact angle measurement for hydrophilicity of  $\text{Ni}/\text{Ni}_{0.8}\text{Mo}_{4.2}\text{N}_6$  and Pt/C.

(LSV) methods. The results in Fig. 3a show the most positive potential for  $\text{Ni}/\text{Ni}_{0.8}\text{Mo}_{4.2}\text{N}_6$  suggesting the highest activity towards HER. At current density of  $10 \text{ mA cm}^{-2}$ , the overpotential of  $\text{Ni}/\text{Ni}_{0.8}\text{Mo}_{4.2}\text{N}_6$  is only  $20 \text{ mV}$ , much lower than those for either  $\text{Ni}_{0.8}\text{Mo}_{4.2}\text{N}_6$  or metallic Ni, and is even  $21 \text{ mV}$  lower than the benchmark Pt/C (20 wt%). The  $\text{Ni}/\text{Ni}_{0.8}\text{Mo}_{4.2}\text{N}_6$  overpotential is found to be reproducible to  $\pm 1.0 \text{ mV}$  (Fig. S8). Fig. S9 shows how the performance of  $\text{Ni}/\text{Ni}_{0.8}\text{Mo}_{4.2}\text{N}_6$  for HER varies with the molar ratio of nickel, and the sample with 48.6 wt% cubic nickel is found to be optimal.

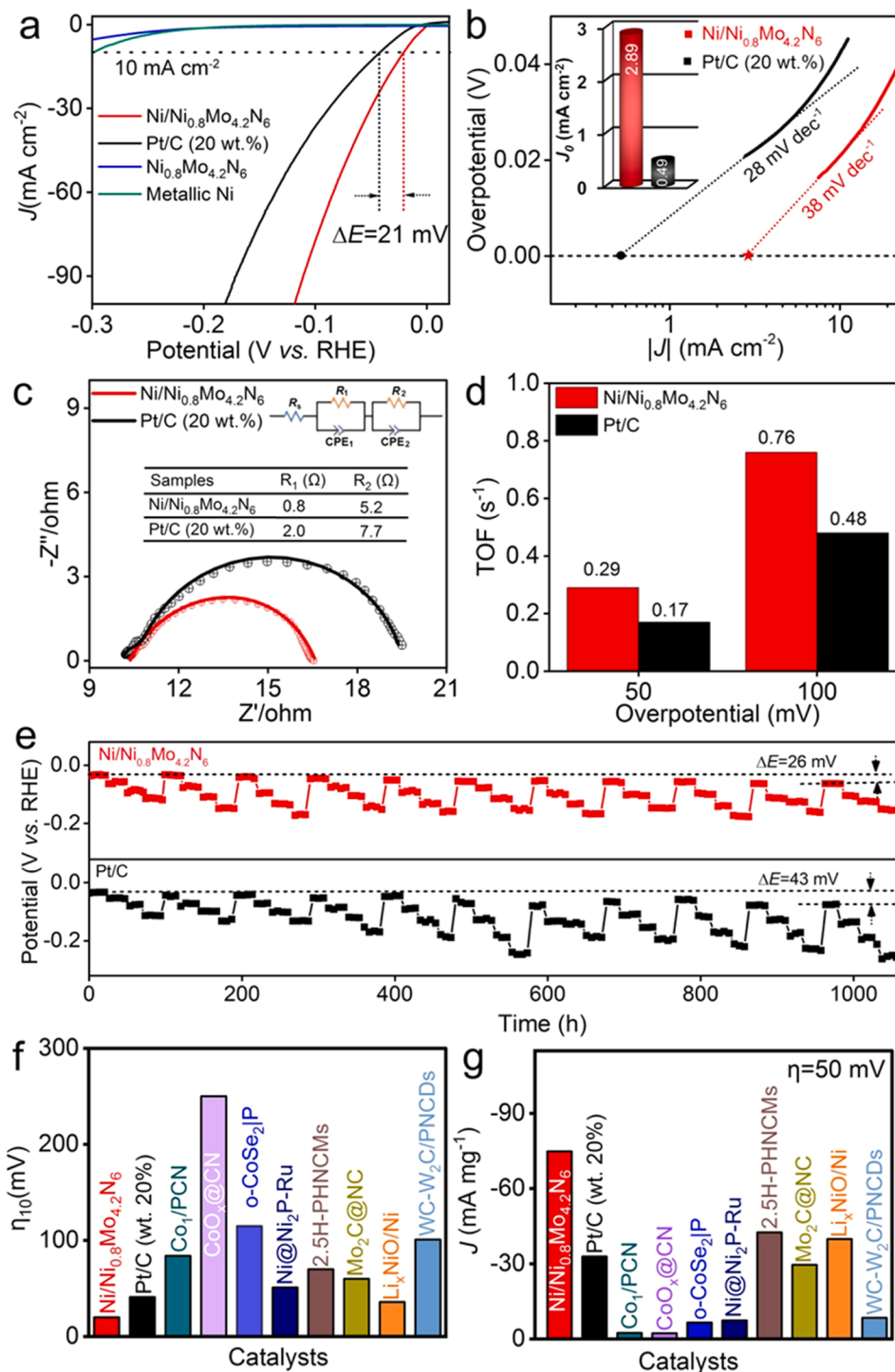
As an inherent property of an electrocatalyst, the Tafel slope is analyzed to reveal the HER mechanism. The Tafel slope for  $\text{Ni}/\text{Ni}_{0.8}\text{Mo}_{4.2}\text{N}_6$  was determined as  $38 \text{ mV dec}^{-1}$  by analyzing the minimum slope of the polarization curve (Fig. 3b). This suggests that the Volmer-Heyrovsky mechanism is responsible for the HER pathway [8, 40]. The step of electrochemical desorption ( $\text{H}_{\text{ads}} + \text{H}_2\text{O} + \text{e}^- \rightarrow \text{H}_2 + \text{OH}^-$ ) is the rate-determining step (RDS) in this mechanism because of the high affinity of Ni for adsorbed  $\text{H}^*$ . The Volmer reaction ( $\text{H}_2\text{O} + \text{e}^- \rightarrow \text{H}_{\text{ads}} + \text{OH}^-$ ) plays a dominant role in activating water for the HER kinetics on both  $\text{Ni}_{0.8}\text{Mo}_{4.2}\text{N}_6$  and metallic Ni. The Tafel slopes of  $\text{Ni}_{0.8}\text{Mo}_{4.2}\text{N}_6$  and metallic Ni are  $180$  and  $123 \text{ mV dec}^{-1}$ , respectively (Fig. S10). By extrapolating Tafel plots to zero overpotential,  $\text{Ni}/\text{Ni}_{0.8}\text{Mo}_{4.2}\text{N}_6$  has a  $J_0$  of  $2.89 \text{ mA cm}^{-2}$ , five times greater than commercial Pt/C ( $0.49 \text{ mA cm}^{-2}$ ). The higher  $J_0$  demonstrates that the intrinsic kinetics of the HER electron-transfer activity on  $\text{Ni}/\text{Ni}_{0.8}\text{Mo}_{4.2}\text{N}_6$  is much faster than for Pt/C [41]. These results are further confirmed by electrochemical impedance spectroscopy (EIS) measurement. As shown in Fig. 3c, the charge transfer resistances for HER on  $\text{Ni}/\text{Ni}_{0.8}\text{Mo}_{4.2}\text{N}_6$  and Pt/C electrodes are  $5.2$  and  $7.7 \Omega$ , respectively. This suggests that HER kinetics occur faster on  $\text{Ni}/\text{Ni}_{0.8}\text{Mo}_{4.2}\text{N}_6$  than on Pt/C. Additionally, the high (metallic) electrical conductivity of  $\text{Ni}/\text{Ni}_{0.8}\text{Mo}_{4.2}\text{N}_6$  gives a resistance of  $0.8 \Omega$  compared to  $2.0 \Omega$  for Pt/C at the same mass loading. The superior conductivity of  $\text{Ni}/\text{Ni}_{0.8}\text{Mo}_{4.2}\text{N}_6$  is advantageous for

electrochemical catalysis to reduce the non-faradaic energy consumption [9]. The exceptional superhydrophilicity of  $\text{Ni}/\text{Ni}_{0.8}\text{Mo}_{4.2}\text{N}_6$  enables the aqueous electrolyte to effectively wet the electrocatalyst, thereby enhancing mass transfer in the HER process.

To determine the inherent electrocatalytic activity of different catalysts, the TOF of each Ni active site is computed by considering the total number of accessible Ni sites (Fig. S11). In Fig. 3d, at overpotentials of  $50$  and  $100 \text{ mV}$ , the respective TOF values for  $\text{Ni}/\text{Ni}_{0.8}\text{Mo}_{4.2}\text{N}_6$  are  $0.29$  and  $0.76 \text{ s}^{-1}$ , compared to  $0.17$  and  $0.48 \text{ s}^{-1}$  for the commercial Pt/C. Hence, in terms of overpotential,  $J_0$  and TOF,  $\text{Ni}/\text{Ni}_{0.8}\text{Mo}_{4.2}\text{N}_6$  outperforms Pt/C as an efficient HER catalyst in alkaline solutions.

The practical applicability of an electrocatalyst heavily relies on its ability to maintain durability, which is a critical parameter that must be taken into consideration. A prolonged electrocatalytic test for hydrogen evolution reaction (HER) was conducted by cycling through four different current densities ( $10$ – $40 \text{ mA cm}^{-2}$ ) within a 24-hour interval. After  $1000 \text{ h}$ , the  $\text{Ni}/\text{Ni}_{0.8}\text{Mo}_{4.2}\text{N}_6$  displays a smaller potential decrease ( $26 \text{ mV}$ ) at  $10 \text{ mA cm}^{-2}$  current density than the commercial Pt/C ( $43 \text{ mV}$ ) in Fig. 3e. The HR-TEM images in Fig. S12 disclose no structural variations for  $\text{Ni}/\text{Ni}_{0.8}\text{Mo}_{4.2}\text{N}_6$  after the durability test, demonstrating structural robustness during alkaline HER electrocatalysis. The Faradic efficiency (FE) of the  $\text{Ni}/\text{Ni}_{0.8}\text{Mo}_{4.2}\text{N}_6$  is determined from the volume of hydrogen evolution (Fig. S13). Experimental results have demonstrated that the efficiency of  $\text{H}_2$  volume production during electrolysis in a  $1.0 \text{ M KOH}$  solution is almost  $100\%$  ( $>99.3\%$ ). This validates that the quantity of electricity passed is directly proportional to the amount of  $\text{H}_2$  generated through the current flow [42–44].

Overall, the above results demonstrate that  $\text{Ni}/\text{Ni}_{0.8}\text{Mo}_{4.2}\text{N}_6$  shows outstanding HER performance, superior to that of Pt/C and other reported state-of-the-art catalysts. Direct comparisons of catalyst overpotentials normalized by electrode surface area, and of mass currents normalized by mass loading of catalyst are shown in Fig. 3f and g, with



further comparison data in Fig. S14 and Table S3.

To investigate the metal-support interactions of Ni and  $\text{Ni}_{0.8}\text{Mo}_{4.2}\text{N}_6$ , we analyzed the charge density distributions and conducted DFT calculations on the intermediate  $\text{H}^*$  adsorption free energies ( $\Delta G_{\text{H}^*}$ ), which are detailed in the [Supporting Information](#). The optimized structures of a Ni cluster,  $\text{Ni}_{0.8}\text{Mo}_{4.2}\text{N}_6$  and  $\text{Ni}/\text{Ni}_{0.8}\text{Mo}_{4.2}\text{N}_6$  are shown in Fig. S15. To investigate the impact of  $\text{Ni}_{0.8}\text{Mo}_{4.2}\text{N}_6$  and Ni on the electronic structure, the density of states (DOS) was calculated and presented in Fig. 4b. All systems exhibited finite DOS values around the Fermi level, indicating their inherent metallic properties. The HOMO of  $\text{Ni}/\text{Ni}_{0.8}\text{Mo}_{4.2}\text{N}_6$  located in close proximity to the Fermi level is closer than that of pure

metallic Ni. This suggests that  $\text{Ni}/\text{Ni}_{0.8}\text{Mo}_{4.2}\text{N}_6$  possess a greater tendency to lose electrons, which weakens the  $\text{H}^*$  adsorption and enhances the HER activity. These findings align with the outcomes from XPS and XANES investigations.  $\text{Ni}/\text{Ni}_{0.8}\text{Mo}_{4.2}\text{N}_6$  shows excellent performance, which is attributed to the low dissociation barrier of water for Ni-based catalyst materials. As shown in Fig. 4c, the energy barrier for breaking the OH-H bond in water is 1.19 eV on Pt (111) surface and such a high energy barrier clearly hinders the dissociation of water to  $\text{H}_{\text{ads}}$  [29]. Strikingly, the dissociation barrier of water is 0.52 eV on  $\text{Ni}/\text{Ni}_{0.8}\text{Mo}_{4.2}\text{N}_6$  surface. Thus, the  $\text{Ni}/\text{Ni}_{0.8}\text{Mo}_{4.2}\text{N}_6$  surface can promote water dissociation substantially and increase the rate of  $\text{H}_{\text{ads}}$  formation. The

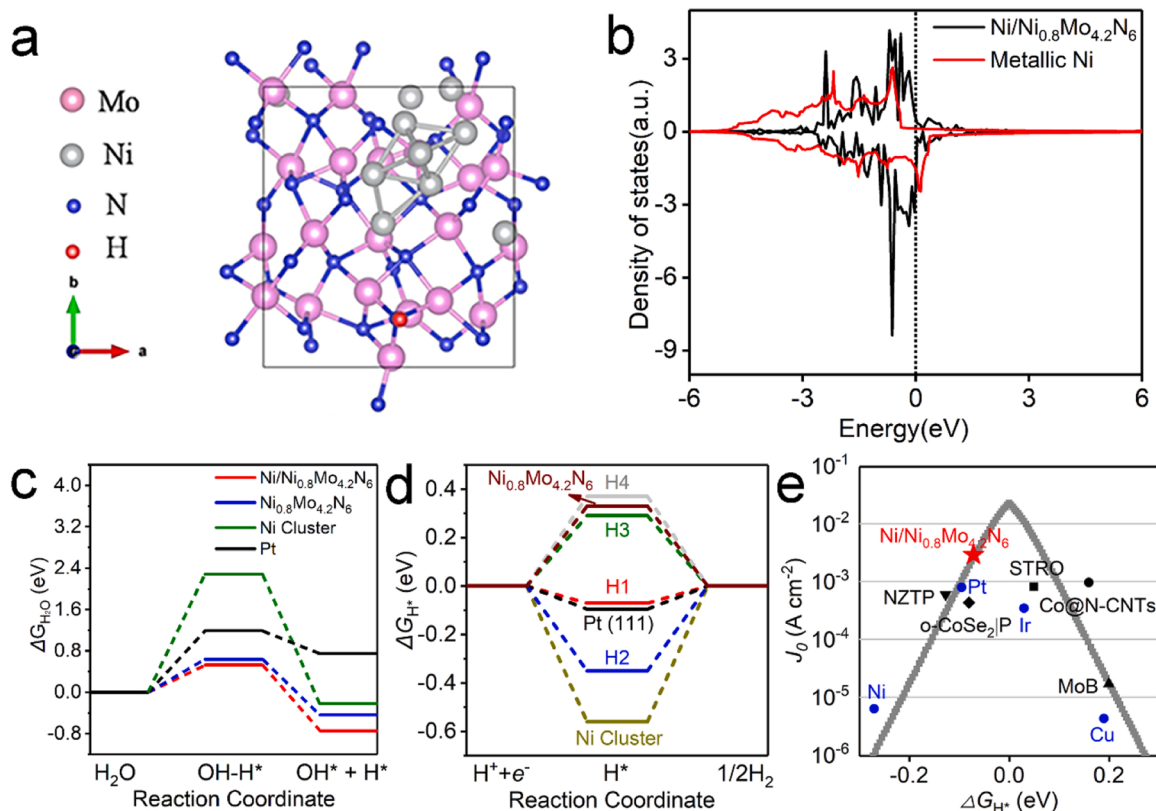


**Fig. 4.** (a) Optimized structures of Ni/Ni<sub>0.8</sub>Mo<sub>4.2</sub>N<sub>6</sub>. (b) Calculated electronic densities of states metallic Ni and Ni/Ni<sub>0.8</sub>Mo<sub>4.2</sub>N<sub>6</sub>. (c) Reaction energy diagram of water dissociation on the Pt (111) surface (black), Ni Cluster (green), Ni<sub>0.8</sub>Mo<sub>4.2</sub>N<sub>6</sub> (blue) and Ni/Ni<sub>0.8</sub>Mo<sub>4.2</sub>N<sub>6</sub> surface (red). The initial state (H<sub>2</sub>O), the transition state (TS) and the final state (H\* + OH\*) are indicated in the diagram with the corresponding energy barrier on the two surfaces. (d) Calculated free-energy diagram of HER over metallic Ni cluster, Pt (111) and Ni/Ni<sub>0.8</sub>Mo<sub>4.2</sub>N<sub>6</sub> at equilibrium potential. (e) Volcano plot of experimentally measured  $J_0$  as a function of the DFT-calculated Gibbs free energy of adsorbed atomic hydrogen. Detailed cited references can be found in Table S3 in the Supporting Information.

Sabatier principle suggests that a site with a moderate Gibbs free energy value ( $\Delta G_{H^*} = 0$  eV) for atomic hydrogen adsorption is optimal for the HER [15]. As shown in Fig. 4d, the calculated  $\Delta G_{H^*}$  on the site of H1 in Ni/Ni<sub>0.8</sub>Mo<sub>4.2</sub>N<sub>6</sub> is  $-0.07$  eV, more close to zero than for Pt. And much larger than the Ni cluster ( $-0.55$  eV) and the Ni<sub>0.8</sub>Mo<sub>4.2</sub>N<sub>6</sub> ( $0.33$  eV) (Fig. S16). This reveals more favorable H\* desorption kinetics on Ni/Ni<sub>0.8</sub>Mo<sub>4.2</sub>N<sub>6</sub> during the HER process. Ni/Ni<sub>0.8</sub>Mo<sub>4.2</sub>N<sub>6</sub> is located near the top of the  $J_0$  vs.  $\Delta G_{H^*}$  volcanic diagram in Fig. 4e, closely resembling state-of-the-art hydrogen electrocatalysts (Table S3). This confirms the outstanding performance of Ni/Ni<sub>0.8</sub>Mo<sub>4.2</sub>N<sub>6</sub>.

#### 4. Conclusions

In conclusion, Ni/Ni<sub>0.8</sub>Mo<sub>4.2</sub>N<sub>6</sub> demonstrates improved catalytic kinetics and offers high activity for HER owing to the strong interaction between the Ni nanoparticle and Ni<sub>0.8</sub>Mo<sub>4.2</sub>N<sub>6</sub>. The combination of surface superhydrophilicity and electron withdrawal reduce the desorption energy of hydrogen on nickel, and allows the Ni/Ni<sub>0.8</sub>Mo<sub>4.2</sub>N<sub>6</sub> electrocatalyst to exhibit impressive ultra-high HER activity with excellent stability over 1000 h in alkaline media. Application of Ni/Ni<sub>0.8</sub>Mo<sub>4.2</sub>N<sub>6</sub> in water splitting, chlorine alkali industry and related electrochemical energy conversion and storage devices is anticipated. Our strategy of engineering catalyst particle local electronic structure through substitution of the same element within the support may also lead to discovery of other outstanding materials for the HER and related electrochemical processes.

#### CRediT authorship contribution statement

**Shuqin Liang:** Investigation, Data curation, Formal analysis,

Writing – original draft. **Huashuai Hu:** Investigation, Formal analysis, Methodology, Writing – original draft. **Jue Liu:** Formal analysis, Writing – original draft. **Hangjia Shen:** Investigation, Methodology. **Qiao Li:** Investigation, Methodology. **Nianxiang Qiu:** Investigation, Methodology. **HaiChuan Guo:** Software, Formal analysis. **Xuyun Guo:** Investigation. **Shiyu Du:** Software, Formal analysis. **Ye Zhu:** Conceptualization. **Jian Liu:** Supervision. **J. Paul Attfield:** Conceptualization, Writing – review & editing. **Minghui Yang:** Supervision, Conceptualization, Writing – review & editing, Funding acquisition.

#### Declaration of Competing Interest

The authors declare that they have no known competing financial interests or personal relationships that could have appeared to influence the work reported in this paper.

#### Data availability

No data was used for the research described in the article.

#### Acknowledgments

M. Yang thank the support from the Natural Science Foundation of China (Grant No. 61971405), Zhejiang National Science Fund for Distinguished Young Scholars (Grant No. R20B010001) and the Fundamental Research Funds for the Central Universities (Grant No. DUT22RC(3)050). S. Du thank the support from the Entrepreneurship Program of Foshan National Hi-tech Industrial Development Zone, Zhejiang Province Key Research and Development Program (Grant No. 2019C01060). The research at ORNL's Spallation Neutron Source

NOMAD beamlines was supported by the U.S. Department of Energy's Office of Basic Sciences Scientific User Facilities Division.

## Appendix A. Supplementary material

Supplementary data associated with this article can be found in the online version at doi:10.1016/j.apcatb.2023.123008.

## References

- [1] M. Hu, B. Liu, H. Chen, X. Xu, P. Jing, X. Guo, R. Yang, X. Wang, R. Gao, J. Zhang, Universal construction of sulfur doped molybdenum-based nanosheets for enhanced hydrogen evolution in a wide pH range, *Appl. Catal. B* 322 (2023), 122131.
- [2] W. Liang, M. Zhou, X. Lin, J. Xu, P. Dong, Z. Le, M. Yang, J. Chen, F. Xie, N. Wang, Y. Jin, H. Meng, Nickel-doped tungsten oxide promotes stable and efficient hydrogen evolution in seawater, *Appl. Catal. B* 325 (2023), 122397.
- [3] P.J. McHugh, A.D. Stergiou, M.D. Symes, Decoupled electrochemical water splitting: from fundamentals to applications, *Adv. Energy Mater.* 10 (2020) 2002453.
- [4] J. Chi, H. Yu, Water electrolysis based on renewable energy for hydrogen production, *Chin. J. Catal.* 39 (2018) 390–394.
- [5] J.K. Norskov, T. Bligaard, A. Logadottir, J.R. Kitchin, J.G. Chen, S. Pandelov, J. K. Norskov, Trends in the exchange current for hydrogen evolution, *J. Electrochem. Soc.* 152 (2005) J23–J26.
- [6] Z.W. Seh, J. Kibsgaard, C.F. Dickens, I. Chorkendorff, J.K. Norskov, T.F. Jaramillo, Combining theory and experiment in electrocatalysis: insights into materials design, *Science* 355 (2017) eaad4998.
- [7] K. Lu, Y. Liu, F. Lin, I.A. Cordova, S. Gao, B. Li, B. Peng, H. Xu, J. Kaelin, D. Coliz, C. Wang, Y. Shao, Y. Cheng, Li<sub>x</sub>NiO/Ni heterostructure with strong basic lattice oxygen enables electrocatalytic hydrogen evolution with Pt-like activity, *J. Am. Chem. Soc.* 142 (2020) 12613–12619.
- [8] J. Chang, Y. Xiao, Z. Luo, J. Ge, C. Liu, W. Xing, Recent progress of non-noble metal catalysts in water electrolysis for hydrogen production, *Acta Phys. Chim. Sin.* 32 (2016) 1556–1592.
- [9] Y. Yuan, J. Wang, S. Adimi, H. Shen, T. Thomas, R. Ma, J.P. Attfield, M. Yang, Zirconium nitride catalysts surpass platinum for oxygen reduction, *Nat. Mater.* 19 (2020) 282–286.
- [10] Z. Li, R. Ma, Q. Ju, Q. Liu, L. Liu, Y. Zhu, M. Yang, J. Wang, Spin engineering of single-site metal catalysts, *Innovation* 3 (2022), 100268.
- [11] Jakob Kibsgaard, I. Chorkendorff, Considerations for the scaling-up of water splitting catalysts, *Nat. Energy* 4 (2019) 430–433.
- [12] K. Zhang, Y. Duan, N. Graham, W. Yu, Unveiling the synergy of polymorph heterointerface and sulfur vacancy in NiS/Ni<sub>3</sub>S<sub>2</sub> electrocatalyst to promote alkaline hydrogen evolution reaction, *Appl. Catal. B* 323 (2023), 122144.
- [13] Y. Hu, Z. Li, Z. Wang, X. Wang, W. Chen, J. Wang, W. Zhong, R. Ma, Suppressing local dendrite hotspots via current density redistribution using a superlithiophilic membrane for stable lithium metal anode, *Adv. Sci.* 10 (2023), e2206995.
- [14] P. Wang, X. Zhang, J. Zhang, S. Wan, S. Guo, G. Lu, J. Yao, X. Huang, Precise tuning in platinum-nickel/nickel sulfide interface nanowires for synergistic hydrogen evolution catalysis, *Nat. Commun.* 8 (2017) 14580.
- [15] J. Zhu, L. Hu, P. Zhao, L.Y.S. Lee, K.Y. Wong, Recent advances in electrocatalytic hydrogen evolution using nanoparticles, *Chem. Rev.* 120 (2020) 851–918.
- [16] X. Shan, J. Liu, H. Mu, Y. Xiao, B. Mei, W. Liu, G. Lin, Z. Jiang, L. Wen, L. Jiang, An engineered superhydrophilic/superaerophobic electrocatalyst composed of the supported CoMoS<sub>x</sub> chalcogel for overall water splitting, *Angew. Chem. Int. Ed.* 59 (2020) 1659–1665.
- [17] T. Wang, M. Wang, H. Yang, M. Xu, C. Zuo, K. Feng, M. Xie, J. Deng, J. Zhong, W. Zhou, T. Cheng, Y. Li, Weakening hydrogen adsorption on nickel via interstitial nitrogen doping promotes bifunctional hydrogen electrocatalysis in alkaline solution, *Energy Environ. Sci.* 12 (2019) 3522–3529.
- [18] W. Ni, T. Wang, P.A. Schouwink, Y.C. Chuang, H.M. Chen, X. Hu, Efficient hydrogen oxidation catalyzed by strain-engineered nickel nanoparticles, *Angew. Chem. Int. Ed.* 59 (2020) 10797–10801.
- [19] T. Bo, Y. Liu, J. Yuan, P. Wu, W. Zhou, Improved photocatalytic HER activity of  $\alpha$ -Sb monolayer with doping and strain engineering, *Appl. Surf. Sci.* 507 (2020), 145194.
- [20] B. You, M.T. Tang, C. Tsai, F. Abild Pedersen, X. Zheng, H. Li, Enhancing electrocatalytic water splitting by strain engineering, *Adv. Mater.* 31 (2019), e1807001.
- [21] J. Zhang, T. Wang, D. Pohl, B. Rellinghaus, R. Dong, S. Liu, X. Zhuang, X. Feng, Interface engineering of MoS<sub>2</sub>/Ni<sub>3</sub>S<sub>2</sub> heterostructures for highly enhanced electrochemical overall-water-splitting activity, *Angew. Chem. Int. Ed.* 55 (2016) 6702–6707.
- [22] C. Zhu, A.L. Wang, W. Xiao, D. Chao, X. Zhang, N.H. Tiep, S. Chen, J. Kang, X. Wang, J. Ding, J. Wang, H. Zhang, H.J. Fan, In situ grown epitaxial heterojunction exhibits high-performance electrocatalytic water splitting, *Adv. Mater.* 30 (2018), e1705516.
- [23] Y. Liu, S. Liu, Y. Wang, Q. Zhang, L. Gu, S. Zhao, D. Xu, Y. Li, J. Bao, Z. Dai, Ru modulation effects in the synthesis of unique rod-like Ni@Ni<sub>2</sub>P-Ru heterostructures and their remarkable electrocatalytic hydrogen evolution performance, *J. Am. Chem. Soc.* 140 (2018) 2731–2734.
- [24] J. Wei, S.N. Qin, J.L. Liu, X.Y. Ruan, Z. Guan, H. Yan, D.Y. Wei, H. Zhang, J. Cheng, H. Xu, Z.Q. Tian, J.F. Li, In situ Raman monitoring and manipulating of interfacial hydrogen spillover by precise fabrication of Au/TiO<sub>2</sub>/Pt sandwich structures, *Angew. Chem. Int. Ed.* 59 (2020) 10343–10347.
- [25] R. Prins, Hydrogen spillover. Facts and fiction, *Chem. Rev.* 112 (2012) 2714–2738.
- [26] S. Wang, Z.J. Zhao, X. Chang, J. Zhao, H. Tian, C. Yang, M. Li, Q. Fu, R. Mu, J. Gong, Activation and spillover of hydrogen on Sub-1 nm palladium nanoclusters confined within sodalite zeolite for the semi-hydrogenation of alkynes, *Angew. Chem. Int. Ed.* 58 (2019) 7668–7672.
- [27] Matthew D. Marcinkowski, April D. Jewell, Michail Stamatakis, Matthew B. Boucher, Emily A. Lewis, Colin J. Murphy, Georgios Kyriakou, E.C.H. Sykes, Controlling a spillover pathway with the molecular cork effect, *Nat. Mater.* (2013) 523–528.
- [28] H. Jin, X. Liu, A. Vasileff, Y. Jiao, Y. Zhao, Y. Zheng, S.Z. Qiao, Single-crystal nitrogen-rich two-dimensional Mo<sub>5</sub>N<sub>6</sub> nanosheets for efficient and stable seawater splitting, *ACS Nano* 12 (2018) 12761–12769.
- [29] F. Lin, Z. Dong, Y. Yao, L. Yang, F. Fang, L. Jiao, Electrocatalytic hydrogen evolution of ultrathin Co-Mo<sub>5</sub>N<sub>6</sub> heterojunction with interfacial electron redistribution, *Adv. Energy Mater.* 10 (2020) 2002176.
- [30] W.F. Chen, K. Sasaki, C. Ma, A.I. Frenkel, N. Marinkovic, J.T. Muckerman, Y. Zhu, R.R. Adzic, Hydrogen-evolution catalysts based on non-noble metal nickel-molybdenum nitride nanosheets, *Angew. Chem. Int. Ed.* 51 (2012) 6131–6135.
- [31] Y. Wang, Y. Sun, F. Yan, C. Zhu, P. Gao, X. Zhang, Y. Chen, Self-supported NiMo-based nanowire arrays as bifunctional electrocatalysts for full water splitting, *J. Mater. Chem. A* 6 (2018) 8479–8487.
- [32] Y. Chen, C. Wang, J. Yu, G. Xiong, H. Niu, Y. Li, D. Sun, X. Zhang, H. Liu, W. Zhou, Underfocus laser induced Ni nanoparticles embedded metallic MoN microrods as patterned electrode for efficient overall water splitting, *Adv. Sci.* 9 (2022) 2105869.
- [33] F. Song, W. Li, J. Yang, G. Han, P. Liao, Y. Sun, Interfacing nickel nitride and nickel boosts both electrocatalytic hydrogen evolution and oxidation reactions, *Nat. Commun.* 9 (2018) 4531.
- [34] J. Neufeld, M. Feygenson, J. Carruth, R. Hoffmann, K.K. Chipley, The nanoscale ordered materials diffractometer NOMAD at the spallation neutron source SNS, *Nucl. Instrum. Methods Phys. Res. Sect. B* 287 (2012) 68–75.
- [35] L. Yu, Q. Zhu, S. Song, B. McElhenney, D. Wang, C. Wu, Z. Qin, J. Bao, Y. Yu, S. Chen, Z. Ren, Non-noble metal-nitride based electrocatalysts for high-performance alkaline seawater electrolysis, *Nat. Commun.* 10 (2019) 5106.
- [36] Y. Li, X. Tan, R.K. Hocking, X. Bo, H. Ren, B. Johannessen, S.C. Smith, C. Zhao, Implanting Ni-O-VO<sub>x</sub> sites into Cu-doped Ni for low-overpotential alkaline hydrogen evolution, *Nat. Commun.* 11 (2020) 2720.
- [37] F. Yang, X. Bao, P. Li, X. Wang, G. Cheng, S. Chen, W. Luo, Boosting hydrogen oxidation activity of Ni in alkaline media through oxygen-vacancy-rich CeO<sub>2</sub>/Ni heterostructures, *Angew. Chem. Int. Ed.* 58 (2019) 14179–14183.
- [38] T. Huhtamaki, X. Tian, J.T. Korhonen, R.H.A. Ras, Surface-wetting characterization using contact-angle measurements, *Nat. Protoc.* 13 (2018) 1521–1538.
- [39] Z. Ni, C. Luo, B. Cheng, P. Kuang, Y. Li, J. Yu, Construction of hierarchical and self-supported NiFe-Pt<sub>3</sub>Ir electrode for hydrogen production with industrial current density, *Appl. Catal. B* 321 (2023), 122072.
- [40] J. Li, H.-X. Liu, W. Gou, M. Zhang, Z. Xia, S. Zhang, C.R. Chang, Y. Ma, Y. Qu, Ethylene-glycol ligand environment facilitates highly efficient hydrogen evolution of Pt/CoP through proton concentration and hydrogen spillover, *Energy Environ. Sci.* 12 (2019) 2298–2304.
- [41] L. Cao, W. Liu, Q. Luo, R. Yin, B. Wang, J. Weissenrieder, M. Soldemo, H. Yan, Y. Lin, Z. Sun, C. Ma, W. Zhang, S. Chen, H. Wang, Q. Guan, T. Yao, S. Wei, J. Yang, J. Lu, Atomically dispersed iron hydroxide anchored on Pt for preferential oxidation of CO in H<sub>2</sub>, *Nature* 565 (2019) 631–635.
- [42] Y. Li, X. Wei, L. Chen, J. Shi, M. He, Nickel-molybdenum nitride nanoplate electrocatalysts for concurrent electrolytic hydrogen and formate productions, *Nat. Commun.* 10 (2019) 5335.
- [43] R. Liu, G. Zhang, H. Cao, S. Zhang, Y. Xie, A. Haider, U. Kortz, B. Chen, N.S. Dalal, Y. Zhao, L. Zhi, C.X. Wu, L.K. Yan, Z. Su, B. Keita, Enhanced proton and electron reservoir reservoir of polyoxometalate grafted on graphene for high-performance hydrogen evolution, *Energy Environ. Sci.* 9 (2016) 1012–1023.
- [44] P. Shen, B. Zhou, Z. Chen, W. Xiao, Y. Fu, J. Wan, Z. Wu, L. Wang, Ruthenium-doped 3D Cu<sub>2</sub>O nanochains as efficient electrocatalyst towards hydrogen evolution and hydrazine oxidation, *Appl. Catal. B* 325 (2023), 122305.